Simulating a Shape Memory Alloy Buoyancy Heat Engine for Undersea Gliders

Alex J. Angilella and Farhan S. Gandhi
Rotorcraft Adaptive and Morphing Structures Lab
Department of Mechanical, Aerospace, and Nuclear Engineering
Rensselaer Polytechnic Institute
Troy, NY USA

Timothy F. Miller
Energy Science and Power Systems Division
The Applied Research Laboratory
The Pennsylvania State University
University Park, PA USA

Undersea gliders are autonomous undersea vehicles (AUVs) that travel the world's oceans in a sawtooth climb-dive pattern. These gliders are driven by buoyancy engines that typically use electrically powered pumps to displace water with an oil bladder and thus enable a buoyancy change. Battery capacity limits the endurance of these types of engines and vehicles. The Argo project uses similar electrical buoyancy engines to help monitor climate change [1]. Increasing the endurance of buoyancy engines could have an impact on sensors deployed in the world's oceans by decreasing the maintenance cost of sensing missions and allowing for studies to be conducted over a longer period of time. Buoyancy heat engines driven by the naturally occurring thermocline that exists over a large expanse of the world's oceans can drastically improve endurance. These engines harness environmental energy as opposed to consuming electrical energy to change vehicle buoyancy. Buoyancy engines have been developed that employ the volume change produced during the phase change of wax [2], but it may also be possible to use the oceanic thermocline to drive a buoyancy heat engine based on shape memory alloys (SMA's) (Fig. 1). Shape memory alloys can recover a large amount of applied strain, up to approximately 10% [3], when heated due to a solid state phase transformation in the alloy. The high strain energy of shape memory alloys can be leveraged to create a lighter and more efficient buoyancy heat engine, but the performance and capability of a solid state SMA based engine is unknown. Previous work has discussed the analysis, design, and testing of such an engine, called the shape memory alloy buoyancy heat engine (SMA-BHE) [4]. This paper will examine the dynamics of the SMA-BHE by coupling a lumped system heat transfer model and the Brinson model for one-dimensional SMA constitutive behavior to the kinematics of a notional undersea glider in an ocean environment. Including the Brinson model and other known SMA relations in the kinematic simulation of a notional glider led to a model that predicted successful AUV operation with a SMA-BHE at depths past 700 m.

Keywords—AUV, glider, shape memory alloy, buoyancy engine

Sponsored by the United States Office of Naval Research

I. INTRODUCTION

The oceanic thermocline has been used to propel an AUV. This was first done with the *Slocum* thermal glider by means of implementing melting wax, various check valves, an oil reservoir, and a bladder [2]. It should also be possible to use the oceanic thermocline to drive a buoyancy heat engine based on SMAs. Understanding the ocean environment in a mathematical sense is crucial to understanding the performance of the SMA-BHE and its interactions with this environment. The undersea environment varies across the globe, and the SMA-BHE was intended to operate within 30^o of the equator. A thermocline exists in these oceans, as well as changes due to density. The variations in these properties are at the heart of this SMA-BHE system. Fig. 1 shows how the temperature varies with depth [5]. At depths less than 10 m in the North Pacific (24^{o}N), the temperature drop is minimal from a high of 25.4^{o}C. Between 10 m and 130 m, the temperature steeply decreases with depth until reaching a knee in the curve and declining at a more moderate rate to another knee in the curve at 770 m. The temperature drop that occurs with increasing depth in the ocean's lower latitudes provides a potential energy difference that can be harnessed to power an undersea engine. The rise and dive behavior of an AUV depends on its buoyant force. Archimedes' principle describes how buoyant force (F_B) depends on the volume of fluid displaced by a body (V_f), the density of the fluid (ρ_w), and the acceleration due to gravity (g) as shown by (1). Fig. 1 also shows how the density of ocean water also changes with depth up to 1 km. This behavior is approximated in (2) and (3). In addition to the temperature change that will be used to drive the vehicle, the change in water density will impact the dynamic behavior of an AUV. The final environmental effect of depth is the hydrostatic pressure of the ocean (P) expressed by (4).

$$F_B = \rho_w V_f g \quad (1)$$

$$\rho_w(x) = 3x + 1025 \text{ for } x <= 1000\ m \quad (2)$$

$$\rho_w(x) = 1028 \text{ for } x > 1000\ m \quad (3)$$

$$P(x) = \rho_w(x) g x \quad (4)$$

This study aims to show that a potentially simple, shape memory alloy (SMA) based system could achieve

978-0-933957-43-5 ©2015 MTS

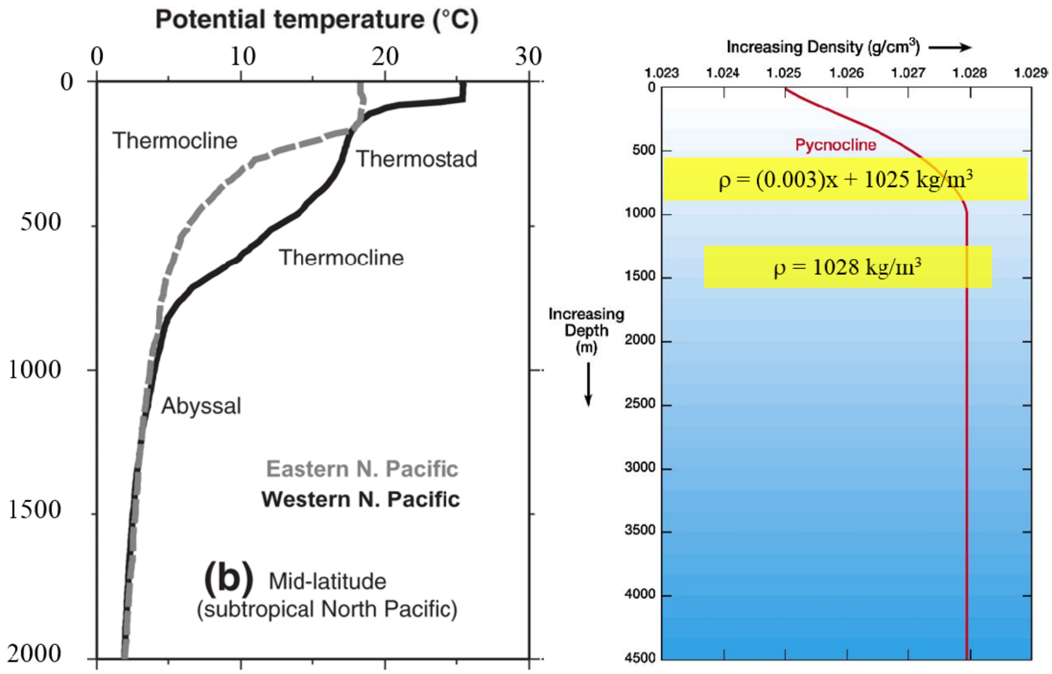

Fig. 1. Thermocline [1] and Pycnocline [14]

similar performance. When heated, shape memory alloys can recover strain that was applied when cool. This is known as the shape memory effect and is due to a solid state phase transformation (between austenite and martensite phases). The shape memory effect opposes, and dominates, the natural inclination of most materials to expand when heated. It is this unconventional behavior that facilitates the creation of a shape memory alloy based buoyancy heat engine. Fig. 2 shows the concept of a shape memory alloy buoyancy heat engine explained and the stages of its deployment. The SMA elements link the buoyancy of the engine to the thermocline. A bias spring is used to prestrain the SMA wires (0 to 1). Upon heating, the wires shrink and compress the bias spring (1 to 2). When cooled again, the bias spring returns the engine to its expanded configuration (2 to 1). This bias spring also provides resistance to a hydrostatic load. This concept was developed into a full prototype shown in Fig. 3 [4]. The maximum amount of recoverable strain is the prestrains introduced to the prototype. Although SMA's are able to recover up to 10% strain, the prototype was limited to 4% prestrain for the sake of extending the fatigue life of the alloy. By design, the SMA wires were located in a wetted shell so that they remained in contact with the surrounding water during operation.

As stated previously, the SMA wires shrink when heated. When deployed at the surface, the SMA-BHE would be in its compressed (austenite) state. The volume reduction of air in the SMA-BHE dry area would cause the AUV to take on water, become negatively buoyant, and sink. As the AUV sinks into cooler waters, the SMA wires would cool to the point that they change phase to martensite. The SMAs are compliant in the martensite phase, and this compliance allows the bias spring to push against the pressure head and displace water, increasing the AUV's buoyancy, and arresting/reversing its descent. In essence, we describe a classic heat engine which would operate between a hot state at the surface and a cold state at a depth of 1km, and perform work (equal to the product of the volume of water displaced and the hydrostatic pressure head). A full discussion of the design and testing of this prototype can be found in [4]. This early prototype was shown to provide an adequate volume change to propel a small AUV, and centered on making the device easy to fabricate and test. This paper focuses on scaling the SMA-BHE prototype technology to a larger size and

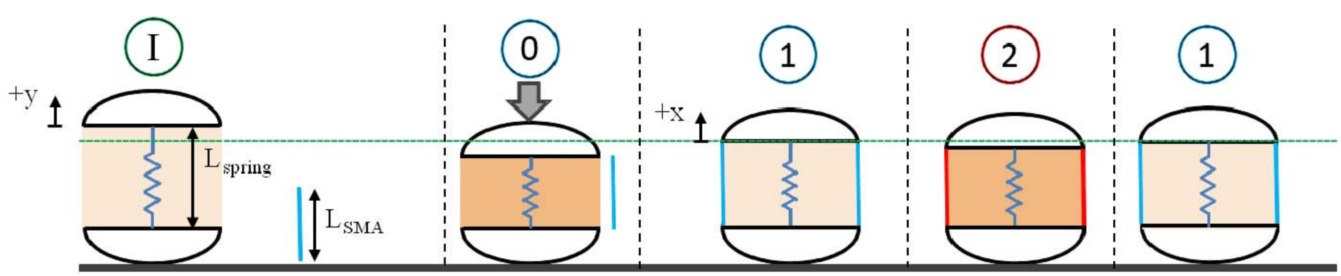

Fig. 2. SMA-BHE Concept

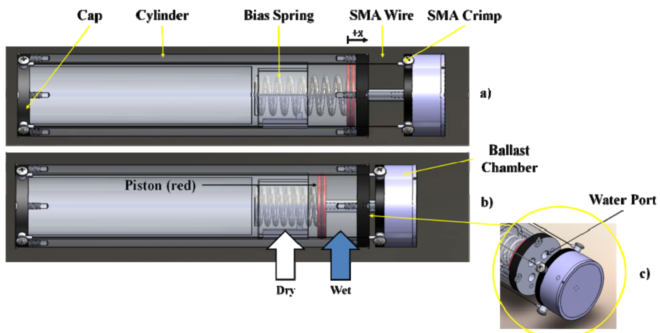

Fig. 3. SMA-BHE Prototype

simulating its behavior in order to explore the design space available for future development.

The thermocline also encapsulates three separate regions of SMA behavior. Because of SMA temperature hysteresis, the heating and cooling transformations that occur during rising and sinking will occur at different temperatures. This hysteresis behavior will be explained later in this paper. At this point, it is important to note three discrete transformation regions for the SMA-BHE within the thermocline; forward, reverse, and inactive. The exact boundaries of these regions are a function of glider and environmental variables that may change over time so it is best to describe the regions by the observable phenomenon that occurs in each region. The forward region (which occurs in deeper, cooler water) encompasses where the SMA-BHE is expanding due to phase transformation and the buoyant force acting on the AUV is increasing. The reverse region (which occurs in warmer, near-surface water) encompasses where the SMA-BHE is shrinking due to phase transformation and the buoyant force acting on the AUV decreases. Between the forward and reverse regions, there is an inactive region where is the SMA-BHE is not transforming due to the SMA temperature hysteresis. In the inactive region, the AUV will accelerate to a terminal velocity. The boundaries for these regions, will be set by the temperature of the SMA wires. The temperature of the SMA wire is determined from the heat transfer to or from the surrounding water and is calculated in the model.

The forward and reverse martensite phase change process has been modeled in multiple ways; phenomenological models based on the observed strain change have been developed, as well as thermodynamic models based on the internal energy or Helmholtz free energy [11]. The Brinson model is an example of a thermodynamic model based on the Helmholtz free energy of a uniaxially loaded shape memory alloy. The Brinson model determines the state of the SMA element by using internal variables to measure the volume fraction of martensite in the SMA. The Brinson model uses a cosine relation to determine the martensite volume fraction as a function of stress and temperature of the SMA element. The model also incorporates additional SMA material properties.

The transformation regions in Fig. 4 are established by the thermocline, and are an example of how an AUV equipped with the SMA-BHE will function differently than an AUV with a high-pressure electrically-driven pump. The SMA-BHE is controlled by its external environment, not an internal trigger, and the lack of external control brings about specific concerns. In the forward transformation region, the SMA elements cool and transform into martensite. Creating a martensite volume fraction builds a potential for volume change. The stress induced martensite volume fraction corresponds to the prestrain that will be recovered when heated. Similarly, the reverse region corresponds to heating that depletes the martensite volume fraction in order to affect a volume change. Although our goal is for the SMA-BHE to be designed so that the martensite and austenite transformations occur within the oceanic thermocline, incomplete transformations can occur due to the phenomena described previously. For example, if the AUV slowly enters the reverse transformation region, a small portion of martensite will form that is enough to arrest the descent of the AUV before the SMA-BHE expands fully. This will lead to a loop of small SMA strains in incomplete transformations where the SMA does not see fully martensitic and fully austenitic states. If SMAs are cycled in incomplete transformations, they undergo what is referred to as partial cycling.

Although it is widely used to model SMA behavior, the Brinson model does not specifically model partial cycling of SMAs and has not been verified for partial cycling. The reader should note that the Brinson model uses cosine functions to determine the martensite volume fractions so that the penetration into a particular transformation region certainly does not linearly correspond the percentage transformation of an alloy. There have been few studies of the behavior of SMA's undergoing partial cycling. Lagoudas et al. investigated 80% and 50% transformations of NiTiCu SMAs,

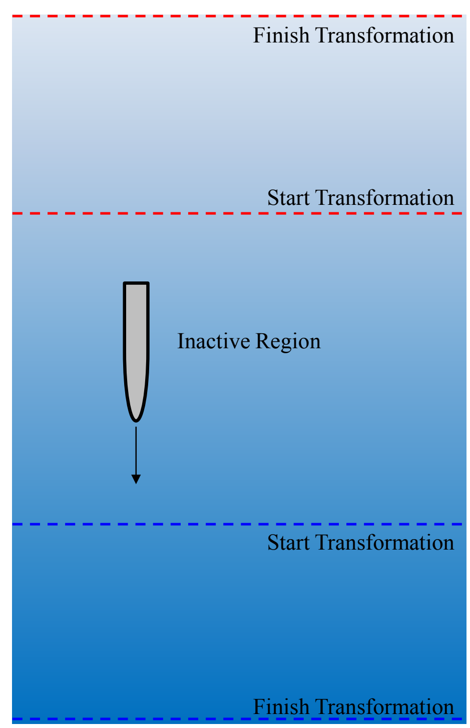

Fig. 4. SMA-BHE Transformation Regions

TABLE I. SLOCUM GLIDER PARAMETERS [9]

Glider Mass (kg)	Glider Length (m)	Glider Diameter (m)	Glider displacement about neutral buoyancy (g)	Maximum Velocity (m/s)
52	2.15	0.21	200	0.40

$$mg - m\ddot{x} - \frac{1}{2}C_D A_C \rho_w(x)\dot{x}^2 - \left[V_0 - \left(\varepsilon_0 - \varepsilon\left(T(x,\dot{x})\right)\right) L_{SMA,0}\right] \rho_w(x) g = 0 \quad (5)$$

conducting a full cycle for 1 in every 1,000 cycles in order to accurately measure strain. Lagoudas found that although there was some residual strain in the SMAs, the transformation strain remained relatively constant. In other words, the transformation strain decayed negligibly over 40,000 cycles [6][7]. Liu also did a similar experiment for NiTi SMAs, but tested for only 80 cycles [8]. Above all, these studies show that the partial thermal cycling of SMAs is phenomenologically similar to full cycling, and thus, and appropriate application for the Brinson model.

Two operational failure modes of the SMA-BHE are of interest; trapped descent and premature arrest. These modes are specifically related to the operation of the SMA-BHE. Trapped descent occurs when the AUV dives deep enough that the hydrostatic pressure head from the ocean prevents the piston in the SMA-BHE from expanding the air volume enough to increase AUV buoyancy to greater than water. The AUV then becomes trapped at depth. The spring stiffness and size of the inactive region determine whether or not the AUV fails in trapped descent. A larger inactive region allows the AUV to accelerate to a greater speed and dive to a deeper depth. The increased depth that is associated with a larger inactive region causes the AUV to experience a larger spring compression that may cause the buoyancy to reduce to less than the buoyancy of water.

The second failure mode of concern is premature arrest, shown in Fig. 5. Where trapped descent is concerned with the AUV traveling too fast, premature arrest is concerned with the AUV traveling too slowly. If the SMA-BHE reaches neutral buoyancy near the border of a transformation region, the AUV achieves a very small depth range. This is highly dependent on the size of the inactive region, the strain at neutral buoyancy, and the maximum speed of the AUV. Fig. 5 depicts two SMA-BHE equipped AUVs with different entry speeds to the forward transformation region. The slow moving AUV is easily stopped by the transformation of a small volume fraction of austenite into martensite. Premature arrest is a soft failure. The AUV will still operate but at a lower depths than it could achieve. Premature arrest is more of an underperformance than a failure and can usually be abated by increasing the strain at which the AUV reaches neutral buoyancy. Whereas premature arrest can occur in either of the transformation regions, trapped descent only occurs in the forward zone.

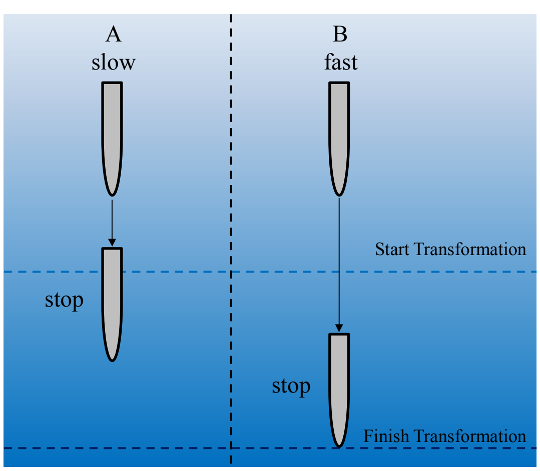

Fig. 5. Premature Arrest

II. MODELING

The simulation used in this paper models the Newtonian mechanics for the vertical transit of an AUV using a shape memory alloy buoyancy heat engine and the heat transfer that enables that motion. To simplify this initial analysis wings were not included and only vertical transit was modeled. As mentioned in the introduction, the temperature and density of the ocean environment is included in the model. Fig. 6 shows a free body diagram of an AUV. Equation 5 is the ordinary differential equation of the force balance that will be integrated to find the depth (x) and velocity. The term A_c is the cross sectional area of the AUV and C_D is the associated drag coefficient, while V_0 is the near surface volume displacement of the glider. Finally, L_{SMA} and ε are the length and strain of the SMA wire, respectively. Increasing depth is defined as positive.

The fourth term in (5) is the buoyant force. The buoyant force is calculated from the temperature of the SMA and the direction of travel by way using the Brinson model (described below). The strain in the martensite phase is ε_0. The dependence of buoyant force on temperature through the SMA is what couples the kinematics to heat transfer in this model. Pressure and friction drag were modeled as well as buoyant force, gravity, inertia, and hydrostatic force on the piston. The hydrostatic force acts on the piston and will compress it to some extent at depth.

The AUV parameters for drag, weight, and size are the same as the *Slocum* glider and are listed in Table I. Modeling the parameters of the *Slocum* glider gave an accurate and experimentally verified drag calculation as well as a benchmark for future SMA-BHE variants. Note that for this work the vehicle was constrained to transit in the vertical direction. Rudnik reported that the coefficient of drag with respect to cross-sectional area for *Slocum* was found to be

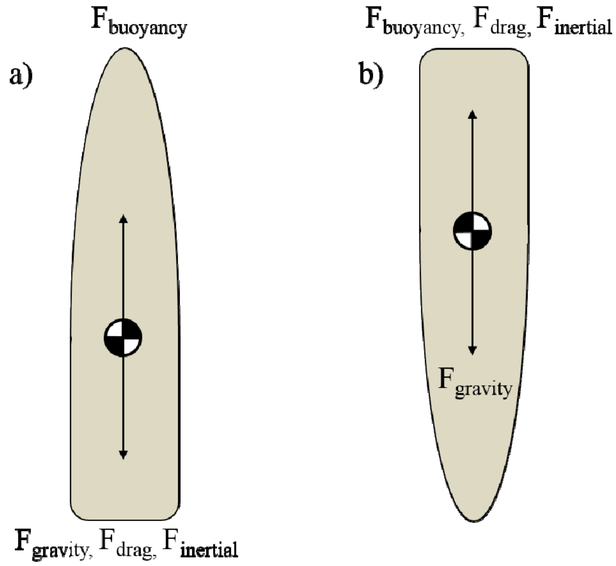

Fig. 6. Free body diagram for a) upward and b) downward accelerating AUV

approximately constant during a tow tank test [9]. The drag values were calculated at zero angle of attack. Once the notional vehicle parameters were set, the engine prototype needed to be scaled to fit the vehicle and provide an adequate buoyancy change. Since the buoyancy change for *Slocum* is known, the engine can be scaled appropriately. The SMA-BHE displacement in the model was set by multiplying the prototype displacement by a scaling parameter to provide +/- 200g of displacement, the displacement change of *Slocum*. Equation 6 describes the Engine Scaling Parameter, which can be thought of as equivalent to packing multiple SMA-BHE's in the vehicle. Secondly, the prototype was not designed to operate against a pressure head [4]. A significant pressure head could compress the bias spring of the early prototype. The amount of compression due to hydrostatic pressure is dependent on the stiffness of the bias spring, though a stiffer bias spring might overload the wires. However, if more SMA wires are added in parallel, the bias spring can be stiffened to reduce pressure so long as the appropriate load per wire was maintained. The spring stiffness was scaled so that the number of SMA's was increased from the 4 in the prototype to 800 in this model. Each wire on the prototype was 12 inches long, which brings the overall SMA mass to 6.18 kg. Concurrent effort is working towards alternative design solutions to reduce this weight. Table II shows the Engine Scaling Parameter and number of wires for two SMA cases that will be discussed in the next paragraph. The number of wires was greater for one case because the vehicle in that case dove to a greater depth and experienced a greater pressure.

$$Engine\ Scaling\ Parameter = \frac{0.4}{\varepsilon_0\ L_{SMA,0}\ A_{piston}\ \rho(0)} \quad (6)$$

Increasing the number of SMA wires and scaling the engine allows the SMA-BHE to operate at significant depth. Drag compounds the concern over the prematurely arrested descent. Excess drag slows the vehicle so that it has less momentum when entering the transformation region. Once the vehicle enters a transformation region it depends on its initial momentum to keep it in motion while the volume change occurs. Reducing drag enables the AUV to descend lower and complete more of the phase transformation. This behavior is analogous to a dynamic mass-spring-damper system. The inertia of the mass helps it compress the spring. Eventually, the spring reverses the direction of mass movement.

With the engine properly scaled and the vehicle parameters set, the SMA-BHE behavior must be added to the model. Typical NiTi SMAs undergo the shape memory effect over a temperature range of 30^{o}C. This shape memory effect is caused by austenite to martensite transformations when cooling (forward) and martensite to austenite when heating (reverse). Each transformation has a start and a finish temperature. This leads to four transformation temperatures; in increasing temperature M_f, M_s, A_s, and A_f. M_s and M_f are the temperatures at which the SMA starts and finishes the reverse transformation from austenite to martensite. A_s and A_f are the temperatures at which the SMA starts and finishes the forward transformation from martensite to austenite. The forward and reverse transformations occur at different temperatures and generally require a change of 10-15^{o}C to complete. The hysteresis of the shape memory effect is measured as the temperature difference between a 50% complete forward transformation and a 50% complete reverse transformation. Typical alloys that demonstrate the shape memory effect are based on Ni-Ti or Cu-Zn. Ni-Ti SMAs were used in the development of the SMA-BHE prototype due to their wide availability. While Ni-Ti alloys are more common, Cu-Zn alloys are inexpensive and have a lower hysteresis than Ni-Ti alloys. Ni-Ti alloys generally have a temperature hysteresis of 30^{o}C, but Cu-Zn alloys can achieve a hysteresis as low as 10^{o}C. Cu-Zn alloys are limited to a maximum strain recovery of 5% [10]. Cu-Zn alloys are also limited to 200 MPa of stress [3]. Ag-Cd and Au-Cd alloys also exhibit low hysteresis transformations, and all of the presented alloys can be tuned to transform over the range of temperatures available in the oceanic thermocline. Due to lack of availability at this time, these low hysteresis SMAs could not be tested in the SMA-BHE prototype.

Two behaviors were modeled to approximate the

TABLE II. AUV PARAMETERS FOR DIFFERENT SMA MODELS

Wire Properties	Engine Scaling Parameter	Number of Wires	Total Wire Mass (kg)	Spring Stiffness (kg/m)	Strain at Neutral Buoyancy
High Hysteresis	16.8	1200	9.27	148,000	0.02
Low Hysteresis	16.8	800	6.18	98,800	0.02

TABLE III. BRINSON MODEL SMA PARAMETERS

Wire Properties	C (MPa/K)	σ_{Ms} (MPa)	σ_{Mf} (MPa)	M_f (°C)	M_s (°C)	A_s (°C)	A_f (°C)
High Hysteresis	15	75	100	5.4	6.4	13.15	14.15
Low Hysteresis	13.8	75	200	5.4	6.4	6.4	10.4

behavior of an SMA appropriate for oceanic application. The SMA used in the prototype required an 80°C temperature difference for a full cycle. As stated previously, the transformations occur over temperature ranges that are separated by a temperature gap that is dependent on the alloy. There are, therefore start and finish temperatures for each transformation; four in total. Fig. 7 and Fig. 8 show two different SMA cycles from the Brinson model. Fig. 7 shows the high hysteresis assumption behavior, and Fig. 8 shows the baseline behavior for low hysteresis. The temperature difference between the point of 50% forward transformation and 50% reverse transformation is the hysteresis. The temperature difference for each transformation affects the temperature change needed for a full cycle, plotted as the dotted lines in Fig. 7 and Fig. 8. The temperature difference required for a transformation is a function of the load on the wire, the transformation temperatures, and the Clausius-Clapeyron coefficient. While bringing the start and finish transformations for the temperatures closer together reduces the temperature difference needed for a transformation; this benefit only goes so far. The Clausius-Clapeyron coefficient is equal to the slope of the dashed lines in Fig. 7 and Fig. 8 that show how the transformation temperatures increase linearly with applied load [11]. This link between the transformation temperatures and the SMA stress ties the Clausius-Clapeyron coefficient to the transformation temperature change. Because the SMA stress increases when the SMA-BHE compresses, the Clausius-Clapeyron coefficient is needed to determine the transformation temperature at this new, increased, stress. An increased Clausius-Clapeyron coefficient decreases the transformation temperature at each stress. Therefore, all other things being equal, an increase in the Clausius-Clapeyron coefficient decreases the overall temperature change needed. Two SMA behavior models were used in the simulation, and the parameters for these models are given in Table III.

The final component of the simulation was heat transfer. When sinking, the SMAs will retain heat and transfer that heat to the cooler water. The heat transfer acts as a negative damper in the dynamic system, slowing the rate of transformation. The combination of the dynamic and heat transfer equations for a mathematical basis for this assertion of negative damping. Equation 11 was derived by substituting the solution for (10) into (5). Strain (ε) is expressed as a function of T_{SMA} in (11). Slowed transformation can either benefit or degrade the system performance. Slowing the rate of transformation will not slow the vehicle. In fact, because the transformation acts to slow the vehicle during both heating and cooling, slowing the transformation rate will cause the vehicle to travel faster. This increased speed will allow the vehicle to build momentum and cover a greater distance than it could with instantaneous heat transfer. There is, however, a potentially negative consequence. If the vehicle travels to greater depths, the AUV could fall victim to a trapped descent. For this reason, it is critical to include convective heat transfer in the model. In order to calculate the convective heat transfer coefficient, h, the laminar flat plate Nusselt number correlation was used for the planform area, Prandtl number, and thermal conductivity of the SMA wire, $A_{planform}$, Pr, and k, respectively. Equations 7-10 define the parameters and relationships used to calculate the heat transfer rate. The Reynolds, Re_L number was calculated with respect to the SMA diameter, D_{SMA} and the dynamic viscosity of water, μ. The temperature of the water, T_w, was interpolated from data gathered from the Western North Pacific curve in Fig. 1. It

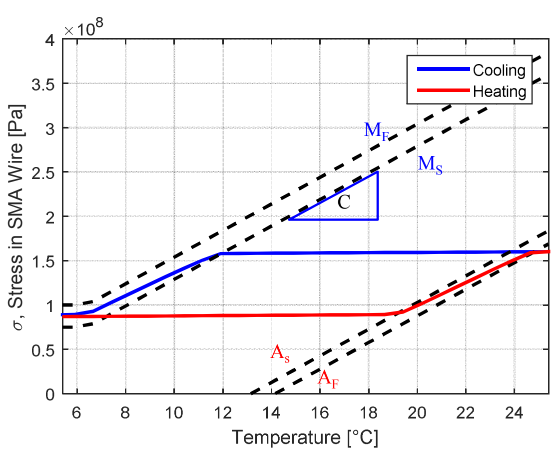

Fig. 7. Simulated stress-temperature path for a full SMA-BHE cycle with a high hysteresis SMA

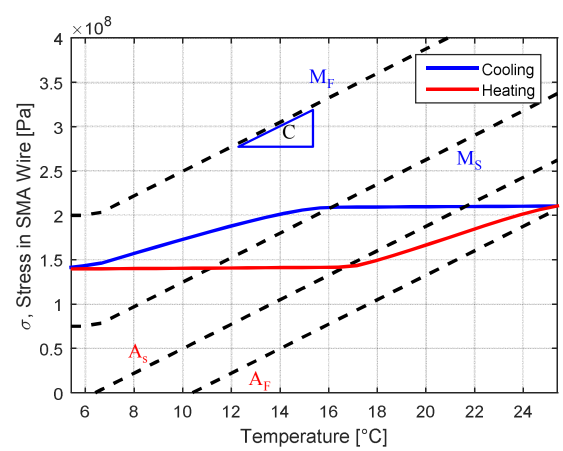

Fig. 8. Simulated stress-temperature path for a full SMA-BHE cycle with a low hysteresis SMA

$$Re_L = \frac{\rho_w(x)\dot{x}D_{SMA}}{\mu} \quad (7)$$

$$h = 0.664\left(\frac{k}{L_{SMA,0}}\right)Pr^{\frac{1}{3}}\sqrt{Re_L} \quad (8)$$

$$\dot{q}(x) = -hA_{planform}(T_{SMA}(x) - T_w(x)) \quad (9)$$

$$T_{SMA}(x) = \frac{q(x)}{m_{SMA}c_p} \quad (10)$$

$$mg - m\ddot{x} - \frac{1}{2}C_D A_C \rho_w(x)\dot{x}^2 + \varepsilon\left(\frac{0.664\left(\frac{k}{L_{SMA,0}}\right)Pr^{\frac{1}{3}}\sqrt{\frac{\rho_w(x)\dot{x}D_{SMA}}{\mu}}A_{planform}(T_{SMA}(x)-T_w(x))\Delta T}{m_{SMA}c_p}\right)L_{SMA,0}\rho_w(x)g$$
$$-(V_0 - \varepsilon_0 L_{SMA,0})\rho_w(x)g = 0,\ where\ \varepsilon = \varepsilon(T) \quad (11)$$

was assumed that the Biot number was sufficiently small, so a lumped-system heat transfer model was used. Equation (9) shows the calculation of the heat transfer rate. Equation 10 describes the heat capacity, q, for a lumped-system body as a function of specific heat, c_p, and SMA mass, m_{SMA}. This model was implemented in a numerical simulation in MATLAB. The Biot number was checked during each iteration of the simulation. The simulation stopped with an error message if either lumped-system assumption or laminar flow assumption was violated.

Numerical integration of the Brinson model presented specific challenges. The numerical solution employed here iteratively solves for the SMA stress and strain level that reaches equilibrium with the bias spring force and the force from hydrostatic pressure. A detailed account of that process was presented in an earlier paper on this project [4]. The Brinson model itself encapsulates two different sets of equations, each are relevant depending on the direction of temperature change. The heating equations depend on the end state of cooling and the cooling equations depend on the end state of the heating. In other words, the differential equation exhibits hysteresis, which only occurred when the vehicle changes directions. This behavior can be referred to as switching. Once the SMAs switch from heating to cooling or cooling to heating, the initial conditions needed to be reset to the SMA state at the switch [11]. Finding the SMA switch state is necessary to model the SMA-BHE cycles, otherwise only a half cycle can be modeled. Chung and Brinson found an arithmetic solution for the switch state, but only if the equilibrium stress-strain is known for every state of the SMA [12]. A different approach was used in the present study in order to obtain more precise values at the end of each transformation. In order to properly integrate the Brinson model and find the switch states, the model was split into two numerical ODE integrations. Each integration represented a half cycle of the SMA (either cooling or heating). The Event Location feature in MATLAB's ODE solver was invoked to find the states at which the vehicle velocity crossed zero, called an event. When the event was located, the dynamic half cycle simulation was ended and the switch state was stored for the next half cycle. After implementing both the half cycle simulation with the Event Location and the heat transfer ODE, the comprehensive model was complete.

III. RESULTS

The dynamic model exerted in this paper is a reasonable approximation of the forces at play during the in-situ operation of a shape memory alloy buoyancy heat engine. Because of the SMA modeling changes, two cases were simulated. Each case represents a different profile for the SMA-BHE due to differences in transformation temperatures and other variables (shown in Table IV). Fig. 7 shows the load path of a high hysteresis case. Note that, at 50% of maximum stress, the hot and cold curves are separated by approximately 13°C. This temperature hysteresis is different, ~10°C, relative to the lower hysteresis case shown in Fig. 8. The smaller temperature range for transformation in Fig. 7 means that the forward and reverse zones in the thermocline are smaller and further apart, creating a larger inactive region. A larger inactive region allows the AUV to accelerate over a longer distance and increase its depth range. The only other difference between the two cases is that the higher hysteresis case occurs at a lower stress state. The lowered stress state is compensated by the addition of more wires.

Fig. 9 and Fig. 10 describe the performance of an AUV using the high hysteresis SMAs. The high hysteresis SMAs powered the AUV to operate between 63.3 m and 729 m at a top speed of 37.8 cm/s. The high hysteresis glider used a 0.88% strain loop, shown in Fig. 10. Point A in Fig. 9 and Fig. 10 is the starting point at which the AUV is placed in the water at the surface. Point B is where the fully compressed SMA-BHE begins to expand. At Point C, the SMA-BHE has

TABLE IV. HIGH AND LOW HYSTERESIS SMA WIRE PARAMETERS

Wire Properties	Depth Range (m)	Temperature Range (°C)	Maximum Speed (cm/s)	Period (hrs)	Fatigue Life (yrs)	Strain Loop
High Hysteresis	63 – 729	6.5 – 24.5	37.8	1.5	169.3	0.88%
Low Hysteresis	71 - 700	7.2 – 23.0	28.5	1.8	204.8	0.6%

stopped expanding because the velocity has dropped to zero. Points D and E describes where the SMA started and stopped contracting due to heating. If the SMA-BHE completed a full cycle, Points A and E would intersect, but the SMA-BHE only fully compresses at the initial point. Fig. 11 shows the results of the dynamic simulation using the low hysteresis SMAs. The first cycle descends the deepest and fastest. The maximum speed is 28.5 cm/s (compare to *Slocum's* maximum speed of 40 cm/s [9]). The maximum depth achieved is 700 m at 7.2^{o}C ocean temperature. The results in Fig. 11 show that, if properly sized, the SMA-BHE can drive an AUV in a steady rise-dive pattern. The strain loop in Fig. 12 shows the SMA strain at each temperature in the AUV cycle. Due to the slow design speed of the AUV, the SMA-BHE is prevented from using the full stroke to drive the cycle. An alternating strain of only 0.6% was sufficient to drive the AUV. In both cases,

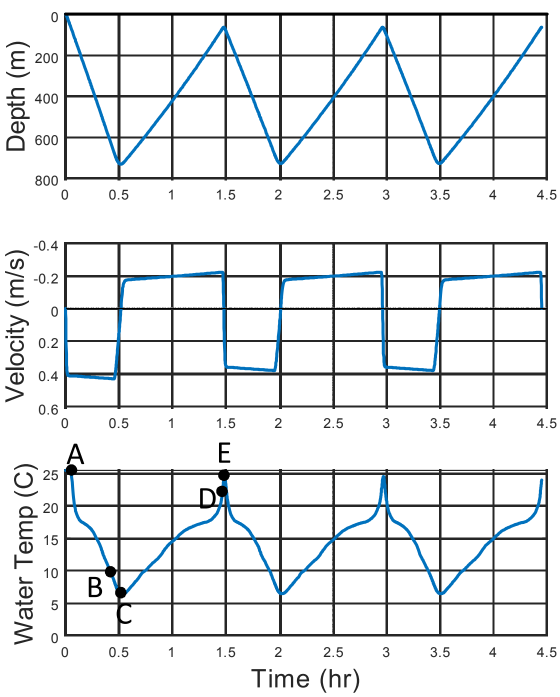

Fig. 9. Dynamic results for high hysteresis SMA

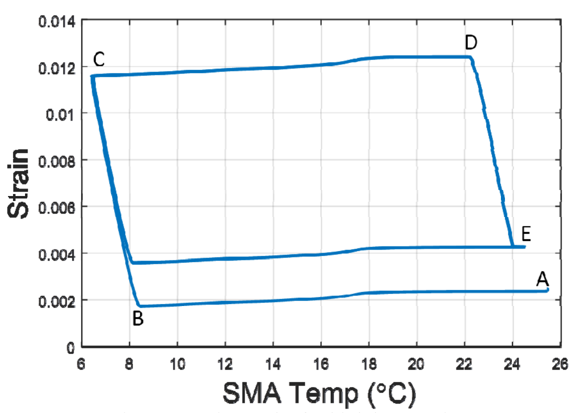

Fig. 10. Strain results for high hysteresis SMA

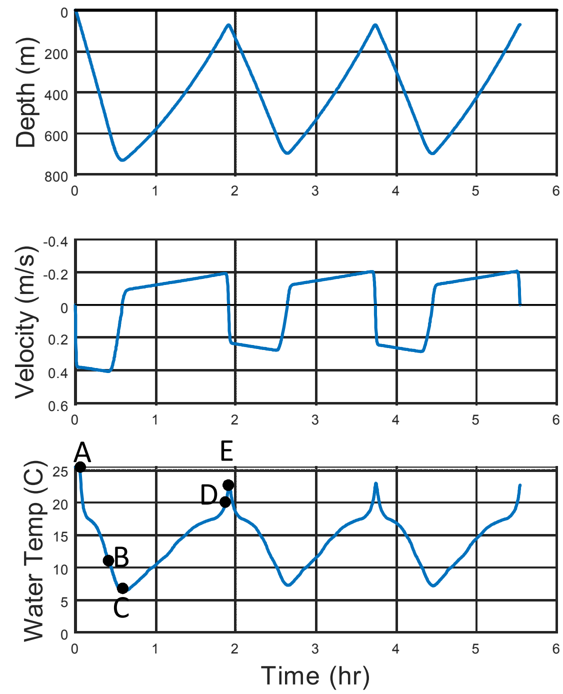

Fig. 11. Dynamic results for low hysteresis SMA

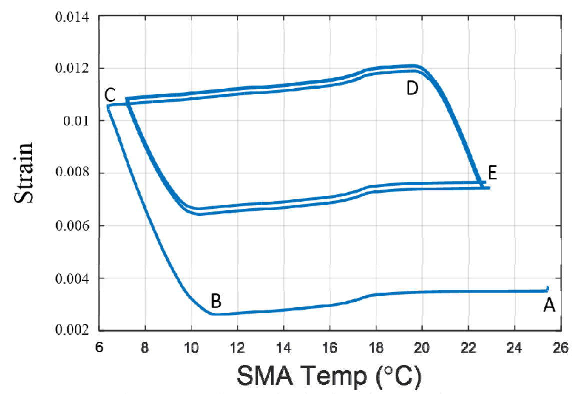

Fig. 12. Strain results for low hysteresis SMA

gliders achieved their maximum speed during descent.

The low strain values are significant for two reasons. First, they shows that a 4% SMA strain is not needed; this suggests that a reduction in maximum SMA strain could be traded to get a greater spring stiffness (per SMA), thereby decreasing the SMA wire weight. Second, research has shown that decreasing SMA transformation strain drastically increases the fatigue life of SMA elements [3], [7], [13]. Experiments at this strain level have shown successful operation up to 10^6 cycles without fatigue failure, and 10^7 cycles is usually given as an upper limit. The simulation gave a cycle period of 1.5 hrs and 1.8 hrs for high and low hysteresis SMAs, respectively. The reader should also note that the engine scaling parameter was based on the maximum buoyancy achieved by the SMA-BHE, 4% in this case. Because the SMA-BHE only partially cycles its SMAs, it developed a buoyancy change that was substantially less than

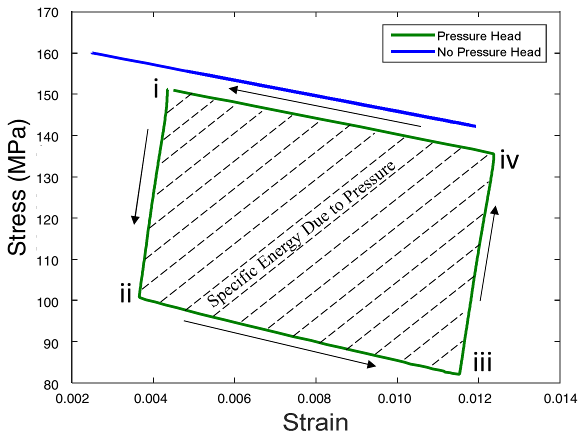

Fig. 13. Energy lost due to hydrostatic pressure

the buoyancy change of *Slocum*, but was sufficient to propel the glider. The results indicate that there is room in the design space for further optimization.

Fig. 13 illustrates the energy stored in the spring due to the hydrostatic pressure. The blue curve shows the stress-strain results from a dynamic simulation that does not act against the oceanic hydrostatic pressure. The stress and strain are in the SMA wires. The green curve bounding the quadrilateral region shows the stress-strain results from when the hydrostatic pressure was added to the model. The increasing compression of the piston due to depth decreases the strain difference in the wire. Additionally, the green curve maps out an area in the stress-strain plane, exhibiting hysteresis. This hysteresis is due to the hydrostatic pressure loading the bias spring and unloading the SMA. At depth, the pressure head unloads the SMA wires so they experience less stress than they would experience at the surface when loaded to the same strain. The SMA stress-strain cycles around the green loop counterclockwise from i to iv. The SMA-BHE dives, fully compressed, from the surface at i to depth at ii. The added hydrostatic pressure compresses the spring and unloads the SMA wires. The SMA wires, therefore, shrink and strain decreases slightly. The large strain change from ii to iii is the forward shape memory transformation. From iii to iv, the SMA-BHE rises to the surface and wire strain increases. Strain increases because the hydrostatic load decreases and more of the load is carried by the wires. The large strain decrease from iv to i is reverse shape memory transformation. This unloading of the SMA explains the hysteresis in Fig. 13.

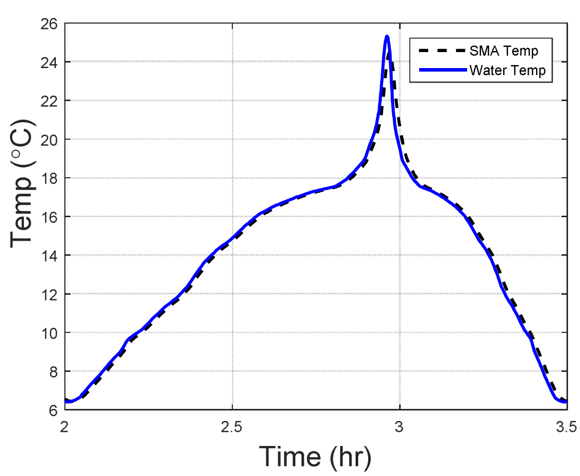

Fig. 14. Temperatures from high hysteresis results

Fig. 14 shows the heat transfer results for the high hysteresis SMA model. The water temperature is shown in the solid blue line. The temperature of the SMA is plotted as a dotted black curve. Overall, the SMA temperature varies little from the water temperature. The maximum temperature difference is 1.9^{o}C at 5.9 hrs for the high hysteresis SMAs. The maximum temperature difference was 1.2^{o}C for the low hysteresis SMA. Both of these points of maximum temperature difference occurred shortly before the minimum depth, and thus, minimum heat transfer. Because the AUV rises slower than it dives, the heat transfer is slower on the rising side of the cycle. The maximum heat transfer will always occur near the surface.

IV. Closing Remarks

A dynamic model was designed to simulate comprehensive and realistic behavior for oceanic operation of a conceptual SMA-BHE. Additionally, SMA wires were identified to operate within the temperature range available in the thermocline. In order to build this model, certain assumptions were made about the behavior of low hysteresis SMAs. The Clausius-Clapeyron coefficient was increased to model the temperature behavior of low hysteresis SMAs such as Cu-Zn-Al. The transformation temperatures used were comparable to literature values. The simulations conducted herein, however, suggest that the SMA-BHE can be adapted for oceanic use and avoid the most general failure modes.

The results showed that heat transfer had a negligible effect on AUV dynamics. However, the depth range of an AUV could be extended by adding resistance to heat transfer. Such is the purview of future work. The maximum depth achieved by the AUV in steady-state oscillation was never more than 729 m. Western North Pacific thermocline data shows a temperature change of 20^{o}C at a depth of 770 m, with minimal temperature change at greater depth. The fact that the knee at 770 m bounded the maximum depth of the AUV is beneficial to the design of the SMA-BHE. If a greater temperature change was needed, the SMA-BHE would be exposed to significantly larger hydrostatic pressure due to the change in the thermocline slope past 770 m. Additional future work concerns achieving a larger volume change per unit mass in order to allow for greater payload. A reduction in volume change per unit mass could be achieved by nonlinear actuation.

V. Acknowledgment

The authors gratefully acknowledge the support of The Office of Naval Research Navy Undersea Research Program (Grant N00014130418 with Dr. Michele Anderson and Maria Medeiros as Program Managers).

References

[1] J. Gould et al, “Argo profiling floats bring new era of in situ ocean observatons,” *EOS Trans. Am. Geophys. Union*, vol. 85, no. 19, pp. 185–191, 2004.

[2] Douglas C. Webb, Simonetti, Paul J., and Jones, Clayton P., “SLOCUM: An Underwater Glider Propelled by Environmental Energy,” *IEE J. Ocean. Eng.*, vol. 26, no. 4, pp. 447–452, Oct. 2001.

[3] Dimitris C. Lagoudas, *Shape Memory Alloys: Modeling and Engineering Applications*. New York, NY: Springer Science+Business Media, 2008.

[4] A. J. Angilella, F. Gandhi, and T. Miller, “Design and Testing of a Shape Memory Alloy Buoyancy Engine for Unmanned Underwater Vehicles,” presented at SciTech2015: 23rd AIAA/AHS Adaptive Structures Conference, Kissimmee, Florida January 2015.

[5] Lynne D. Talley, George L. Pickard, William J. Emery, and James H. Swift, *Descriptive Physical Oceanography: An Introduction*, 6th ed. Academic Press, 2011.

[6] D. C. Lagoudas, C. Li, D. A. Miller, and L. Rong, “Thermomechanical transformation fatigue of SMA actuators,” in *SPIE’s 7th Annual International Symposium on Smart Structures and Materials*, 2000, pp. 420–429.

[7] O. W. Bertacchini, D. C. Lagoudas, and E. Patoor, “Fatigue life characterization of shape memory alloys undergoing thermomechanical cyclic loading,” in *Smart Structures and Materials*, 2003, pp. 612–624.

[8] Y. Liu, J. Laeng, T. V. Chin, and T. Nam, “Partial thermal cycling of NiTi,” *J. Alloys Compd.*, vol. 449, no. 1–2, pp. 144–147, Jan. 2008.

[9] D. L. Rudnick, R. E. Davis, C. C. Eriksen, D. M. Fratantoni, and M. J. Perry, “Underwater gliders for ocean research,” *Mar. Technol. Soc. J.*, vol. 38, no. 2, pp. 73–84, 2004.

[10] Darel E. Hodgson, Ming H. Wu, and Robert J. Biermann, “Shape Memory Alloys,” *ASM Handbook*, vol. 2, 23 vols., ASM International, 1990, pp. 897–902.

[11] L. C. Brinson, “One-Dimensional Constitutive Behavior of Shape Memory Alloys: Thermomechanical Derivation with Non-Constant Material Functions and Redefined Martensite Internal Variable,” *J. Intell. Mater. Syst. Struct.*, vol. 4, no. 2, pp. 229–242, Apr. 1993.

[12] J.-H. Chung, J.-S. Heo, and J.-J. Lee, “Implementation strategy for the dual transformation region in the Brinson SMA constitutive model,” *Smart Mater. Struct.*, vol. 16, no. 1, pp. N1–N5, Feb. 2007.

[13] D. C. Lagoudas, D. A. Miller, L. Rong, and P. K. Kumar, “Thermomechanical fatigue of shape memory alloys,” *Smart Mater. Struct.*, vol. 18, no. 8, p. 085021, Aug. 2009.

[14] Jennifer Bergman, “Density of Ocean Water - Windows to the Universe,” *Density of Ocean Water*, 31-Aug-2001. [Online]. Available: http://www.windows2universe.org/earth/Water/density.html. [Accessed: 23-Jul-2015].